Ceramics International 44 (2018) 17290–17297

Contents lists available at ScienceDirect

Ceramics International

journal homepage: www.elsevier.com/locate/ceramint

Influence of order-disorder effects on the magnetic and optical properties of $NiFe_2O_4$ nanoparticles

Walmir E. Pottker[a], Rodrigo Ono[a], Miguel Angel Cobos[b,c], Antonio Hernando[b,c], Jefferson F.D.F. Araujo[d], Antonio C.O. Bruno[d], Sidney A. Lourenço[a], Elson Longo[e], Felipe A. La Porta[a,*]

[a] Federal Technological University of Paraná, UTFPR, Avenida dos Pioneiros 3131, 86036-370, Londrina, PR, Brazil
[b] Instituto de Magnetismo Aplicado, UCM-ADIF-CSIC, A6 22,500km, 28230 Las Rozas, Spain
[c] Dto. Física Materiales, UCM, Ciudad Universitaria, 28040 Madrid, Spain
[d] Department of Physics, Pontificia Universidade Catolica do Rio de Janeiro, Rio de Janeiro 22451-900, Brazil
[e] Departamento de Química, UFSCar, PO Box 676, 13565-905 São Carlos, SP, Brazil

ARTICLE INFO

Keywords:
Co-precipitation Synthesis
Nickel Ferrite
Magnetic and Optical Properties

ABSTRACT

In this study, we focused on the influence of structural order-disorder effects on the magnetic and optical properties of single-phase nickel ferrite ($NiFe_2O_4$) nanoparticles that, were synthesized by the co-precipitation method and subsequently calcined at 700, 800, 900 and 1000 °C for 120 min in ambient atmosphere. These results from X-ray diffraction and transmission electron microscopy confirm that the $NiFe_2O_4$ nanoparticles have an inverse spinel structure with high purity and crystallinity. The average particle size range between 12 nm and 42 nm depending on the calcination temperature. An analysis of the hysteresis loops revealed a ferromagnetic behavior with an increase in saturation magnetization to 13.2 emu/g from 8.2 emu/g at room temperature. At 7 K, the nanoparticles exhibited saturation magnetization of about 18.1–19.8 emu/g and change in crystallite size, as the calcination temperature increased. UV–vis diffuse spectra results showed an increase in the direct band gap in the range 1.35–1.43 eV, likely due to the increased crystallinity of the $NiFe_2O_4$ nanoparticles. Photoluminescence spectroscopy revealed a strong emission in the visible region, which can easily be attributed to the presence of structural disorders in the [FeO_6], [FeO_4], and [NiO_6] clusters of the $NiFe_2O_4$ powders. Finally, it was found that these $NiFe_2O_4$ powders as-prepared have oxygen atoms that occupy different positions and are highly disturbed in the $NiFe_2O_4$ lattice. These findings provide insights into the magnetic and optical behavior of $NiFe_2O_4$ spinel nanocrystals, with a significant emphasis on structural order-disorder effects, and help reveal the relationship between structure and properties at the atomic level.

1. Introduction

Spinel ferrites nanocrystals have excellent electrical and magnetic properties, and show great potential for use in many technological applications, such as in magnetic recording media [1], photoelectric devices [2], sensors [3] magnetic pigments [4], as well as, photocatalyst for the degradation of various dyes [5–7]. This work highlights the importance of understanding and controlling nanostructures properties. Particularly, the properties of nanoscale materials are usually very different from their bulk form, have enabled the emergence of new technologies [8–12]. In this sense, the properties of spinel ferrites with the formula MFe_2O_4, where M represents a divalent metal ion, depend strongly on the particle size or the surface/volume ratio [13,14]. Among the different type of ferrites, nickel ferrites ($NiFe_2O_4$) are particularly known as soft magnetic semiconducting materials with typical ferromagnetic properties, low conductivity, high chemical stability, and catalytic behavior [15–17]. $NiFe_2O_4$ is known to crystallize in an inverse spinel structure, in which the ferric ions are equally distributed in octahedral [FeO_6] and tetrahedral [FeO_4] clusters, while the nickel ions are distributed only in the octahedral [NiO_6] clusters [16,18]. A broad range of synthetic strategies has been extensively used to obtain spinel ferrites nanocrystals: these include sol-gel [19], co-precipitation [20], microwave plasma [21], microemulsion [22], mechanical alloying [23], auto-combustion [24], hydrothermal [25], and so on. The physical and chemical behavior of the nanocrystals is known to depend on the synthesis procedure used and can be strongly influenced by structural order-disorder effects [26]. These nanocrystals are routinely prepared by different synthetic methods and exhibit different

* Corresponding author.
E-mail addresses: felipe_laporta@yahoo.com.br, felipelaporta@utfper.edu.br (F.A. La Porta).

https://doi.org/10.1016/j.ceramint.2018.06.190
Received 11 June 2018; Received in revised form 14 June 2018; Accepted 23 June 2018
Available online 27 June 2018

structural characteristics at short-, medium- and/or long-range. At the same time, a detailed understanding of structural order-disorder effects in crystalline materials, in principle, it would allow us to link their properties to the structure. This aspect of nanocrystal is useful in the design of improved systems used in different technological applications, and plays an important role in allowing for adjustments in their physical and chemical properties at the nanoscale.

In this study, we focused on the influence of structural order-disorder effects on the magnetic and optical properties of single-phase $NiFe_2O_4$ nanocrystals, which were synthesized by the co-precipitation method and subsequently calcined at diferent temperatures: 700, 800, 900 and 1000 °C for 120 min in ambient atmosphere. The crystalline structure, degree of polydispersity, morphologies, size distributions and the magnetic behavior of $NiFe_2O_4$ nanocrystals as-prepared were investigated by means of X-ray diffraction (XRD) with Rietveld refinement, transmission electron microscopy (TEM), diffuse-reflectance spectroscopy in the ultraviolet–visible region (DRS/UV–vis), photoluminescence (PL) and magnetic property measurements. These findings can provide insights into the magnetic and optical behavior of $NiFe_2O_4$ spinel nanocrystals, with a significant emphasis on structural order-disorder effects, and help reveal the relationship between structure and properties at the atomic level.

2. Experimental methods

2.1. Materials

Nickel (II) chloride hexahydrate (99%), iron (III) chloride hexahydrate (97%), nickel(II) nitrate hexahydrate (98,5%), iron (III) nitrate nonahydrate (98%) were procured from Sigma Aldrich. Sodium hydroxide (analytical grade) was purchased from Merck. All reagents were used without further purification.

2.2. Synthesis of $NiFe_2O_4$ nanocrystals

$NiFe_2O_4$ nanoparticles were prepared by the co-precipitation method in accordance with reported standard protocol [27]. Briefly, 2.5 mmol of $NiCl_2{\cdot}6H_2O$ and 5 mmol of $FeCl_3{\cdot}6H_2O$ were separately dissolved in 50 mL of water. Both solutions were heated at 50 °C and mixed with a stoichiometric ratio (Ni^{2+}: Fe^{3+}) of 1:2. A solution of 100 mL of NaOH (3 M) at 95 °C was used as the precipitating agent. Metal chloride and NaOH solutions were added drop wise from two separate burets into a reaction vessel containing 100 mL of distilled water to obtain uniform particle size distribution [28]. The synthesis temperature was maintained at 80 °C for 120 min under magnetic stirring. The mixture was then cooled to room temperature, magnetically separated, and then washed several times with distilled water in a sonication method. The temperature was then increased to 90 °C to remove the water until dry solid precursor was obtained. The dried precursor was finally calcined in a box-furnace at four different temperatures 700 °C (NC700), 800 °C (NC800), 900 °C (NC900) and 1000 °C (NC1000) for 120 min in air.

2.3. Materials characterization

Structural characterization and the average crystallite size were measured by XRD using Cu-K_α radiation ($\lambda = 0.154178$nm) in a PANalytical X'Pert Pro MPD diffractometer operating in the Bragg Brentano geometry. The data were collected at room temperature in the 2θ range $10° - 100°$ in steps of 0.02°. To identify the phase composition of the samples, the structural data from the International Centre for Diffraction Data (ICDD) was used. The XRD patterns were also subjected to a quantitative analysis by the Rietveld method [29], using the FullProf program [30]. The mean crystallite sizes of the samples were calculated based on the spinel structures of the $NiFe_2O_4$ nanocrystals by applying peak broadening of the (311) peak using Scherrer's formula as seen in Eq. (1):

$$D = \frac{0.9\lambda}{\beta\cos\theta} \quad (1)$$

where D is the mean crystallite size, λ is the Cu-K_α radiation, β is the full width at half maximum (FWHM) in radians and θ is the correspondent Bragg diffraction angle in radians. To further investigate particle size and shape and the Ni/Fe/O molar ratio the $NiFe_2O_4$ samples were observed by a TEM (JEOL, JEM 2100 F) operated at 200 keV and coupled with an energy-dispersive spectrometry (EDS) analysis. TEM images were also used to study the mean particle size distribution from a count of about 100 particles (i.e., with good surface contour) by means of the ImageJ software.

To measure the DC magnetic field, a low-cost, portable Hall magnetometer probe was employed (For further details on how the Hall probe used in this study was build, see the ref. [31]). Magnetization measurements of the samples as-prepared were undertaken using the Hall magnetometer probe with a maximum applied field of 9 kOe at 300 K and 7 K.

Optical properties were observed through DRS/UV–vis and PL measurements. DRS/UV–vis spectra were recorded employing a Cary 5 G spectrophotometer (Varian, USA). PL spectra were obtained at room temperature in atmosphere air using a Thermal Jarrel-Ash Monospec monochromator and a Hamamatsu R446 photomultiplier. A krypton ion laser (Coherent Innova) of wavelength 350.7 nm (3.54 eV) was used as an excitation source; its maximum output power was maintained at 500 mW, and the beam that strikes the sample after passing through an optical chopper has a maximum power of 40 mW.

3. Results and discussion

3.1. Structure and morphology properties

Fig. 1 shows the XRD patterns of the $NiFe_2O_4$ powders prepared by the co-precipitation method and subjected to calcination at different temperatures 700, 800, 900 and 1000 °C for 120 min in ambient atmosphere. The XRD pattern containing the diffraction peaks can be indexed to cubic spinel structure with the space group Fd-3 m (ICDD card N° 086–2267). No characteristic impurity peaks were observed in the samples, indicating that all the crystals exposed to calcination are structurally ordered over the long-range. Clearly, we see that the diffraction peaks are significantly broadened because of the very small crystallite size. The crystallite size calculated from the (311) peak for the $NiFe_2O_4$ powders as-prepared varies from 7.4 nm to 30.1 nm, as a function of the calcination temperature (see Table 1). In addition, we observe sharp and well-defined diffraction peaks as calcination temperature increases, indicating a high degree of crystallinity in these samples as well as an increase in particle size. These results are consistent with the literature [32–34]. In order to confirm the pure and feature a single-phase $NiFe_2O_4$ obtained as well as structural changes as a function of the calcination temperature the Rietveld refinement method was employed (see Fig. 1 and Table 1). The Rietveld refinement parameters obtained for the $NiFe_2O_4$ structures are reported in Table 1, and are very close to those published in the literature [35–37].

However, it is noted that these $NiFe_2O_4$ powders as-prepared, particularly have the oxygen atoms occupy different positions in the lattice. Hence, this fact reveals a certain degree of structural disorder in these samples that, in turn, are probably due to the existence of the oxygen vacancy in these crystalline structures. In other words, this significant variation in the positions of the oxygen atoms can in principle lead to the formation of disorder on the [FeO_6], [FeO_4] and [NiO_6] clusters that in turn are highly distorted in the $NiFe_2O_4$ lattice. This behavior can in principle be related to the structural changes at short-, medium- and long-range, and hence has a great impact on their chemical and physical properties of such materials at the nanoscale.

Based on experimental lattice parameters obtained from the

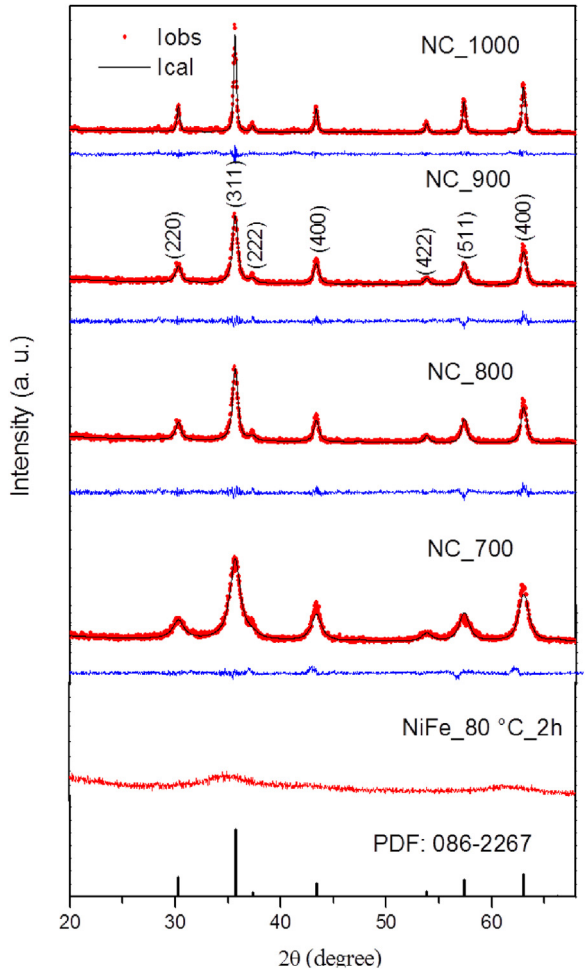

Fig. 1. XRD pattern of NiFe2O4 synthetized at 80 °C for to 120 min and calcinated at 700 °C, 800 °C, 900 °C and 1000 °C.

Rietveld refinement method, were calculated theoretical density (ρ_x) of the NC700, NC800, NC900, and NC1000 samples, according to the following equation [38,39]:

$$\rho_x = \frac{8M}{Na^3} \quad (2)$$

where M is the molecular weight of $NiFe_2O_4$ and N is Avogadro's constant, and a is as-calculated lattice parameter by standard Rietveld technique (see Table 1). The values are comparable to the value of 5.37 g/cm^3 of bulk nickel ferrite [38,39]. While the hopping length between the magnetic ions (the distance between the magnetic ions) in both tetrahedral (A) and octahedral (B) clusters of $NiFe_2O_4$ nanoparticles annealed at different temperature are calculated from the Eqs. (3) and (4) [38,39]:

$$d_A = \frac{a\sqrt{3}}{4} \quad (3)$$

$$d_B = \frac{a\sqrt{2}}{4} \quad (4)$$

where d_A is hopping length for the tetrahedral clusters and d_B is hopping length for the octahedral clusters. The d_A and d_B values of $NiFe_2O_4$ calcination between 700 °C and 1000 °C are presented in Table 1. The length (d_A and d_B) between the magnetic ions and lattice parameter in the $NiFe_2O_4$ does not change with the increase of calcination temperature which collaborates toward the elucidation of the magnetic properties (low saturation magnetization).

Fig. 2(a-e) presents the TEM images with corresponding selected area electron diffraction (SAED) patterns of $NiFe_2O_4$ nanoparticles. TEM images were used to explore the particle morphologies, size distributions as well as the crystallographic properties of the $NiFe_2O_4$ samples, and reveal the formation of crystalline agglomerate with irregular morphologies that drastically changes with the increasing of calcination temperature. In addition, particularly the position and intensities of lines in the SAED pattern indicated that these nanoparticles as-prepared are polycrystalline, as well as, confirm a high purity of the single-phase $NiFe_2O_4$ spinel structure, in a very good accordance with respect to the XRD results.

In the samples synthesized by co-precipitation method, the crystallite size < D311 > is smaller than the largest particle size on the differences of both characterization techniques: XRD and TEM. The first measures one measures the coherent diffraction range size; the larger the crystallite size, the more intense are the diffraction peaks, and, thus, the average crystallite size has different contribution from the small and large particles. Moreover, TEM images can discriminate the different particle sizes. Therefore, in the case of a heterogeneous distribution, crystallite size is an average of the largest and the smallest particles sizes, and it can be smaller than the largest particle size. From the TEM results presented, a semi-empirical relationship was used to estimate the surface area of these nanoparticles using the following Eq. (5):

$$S_{TEM} = \frac{6}{d\rho_X} \quad (5)$$

where S_{TEM} is the surface area, d is average particle size and ρ_x is the theoretical density. In particular, the surface area analysis calculated from TEM decreases with the increase of thermal annealing (see Table 1). In addition, the EDS pattern analysis was also measured to determine the chemical composition as well as the profile elemental distribution of the $NiFe_2O_4$ samples. Therefore, the peak quantification produced a ratio of Ni/Fe/O which is in excellent agreement with the stoichiometry of $NiFe_2O_4$ spinel structure by the EDS pattern analysis (see Table 2).

3.2. Magnetic properties

To probe the magnetic properties of these $NiFe_2O_4$ nanoparticles as-prepared, in particular, the magnetizations (M) versus field (H) loops were recorded at room temperature and 7 K with an applied magnetic

Table 1
The values of the refined lattice parameters, unit cell volume, crystalline size, theoretical density, distance between the magnetic ions, average grain size and surface area of these NiFe2O4 samples as-prepared.

	Lattice Parameters			Particle Size				
Samples	Lattice constant a (Å)	Volume (Å^3)	X-ray Density (g/cm^3)	dA (Å)	dB (Å)	Crystallite size < D_{311} > (nm)	Average particle size (d) (nm)	Surface area (STEM) (m^{2}g^{-1})
NC700	8.3361	579.296	5.37	3.609	2.9470	7.4	12.4(6)	89.67
NC800	8.3346	578.977	5.38	3.609	2.9467	13.7	25.4(6)	43.80
NC900	8.3346	578.987	5.38	3.609	2.9467	19.7	26.0(6)	42.79
NC1000	8.3349	579.034	5.38	3.609	2.9468	30.1	42.3(5)	26.36

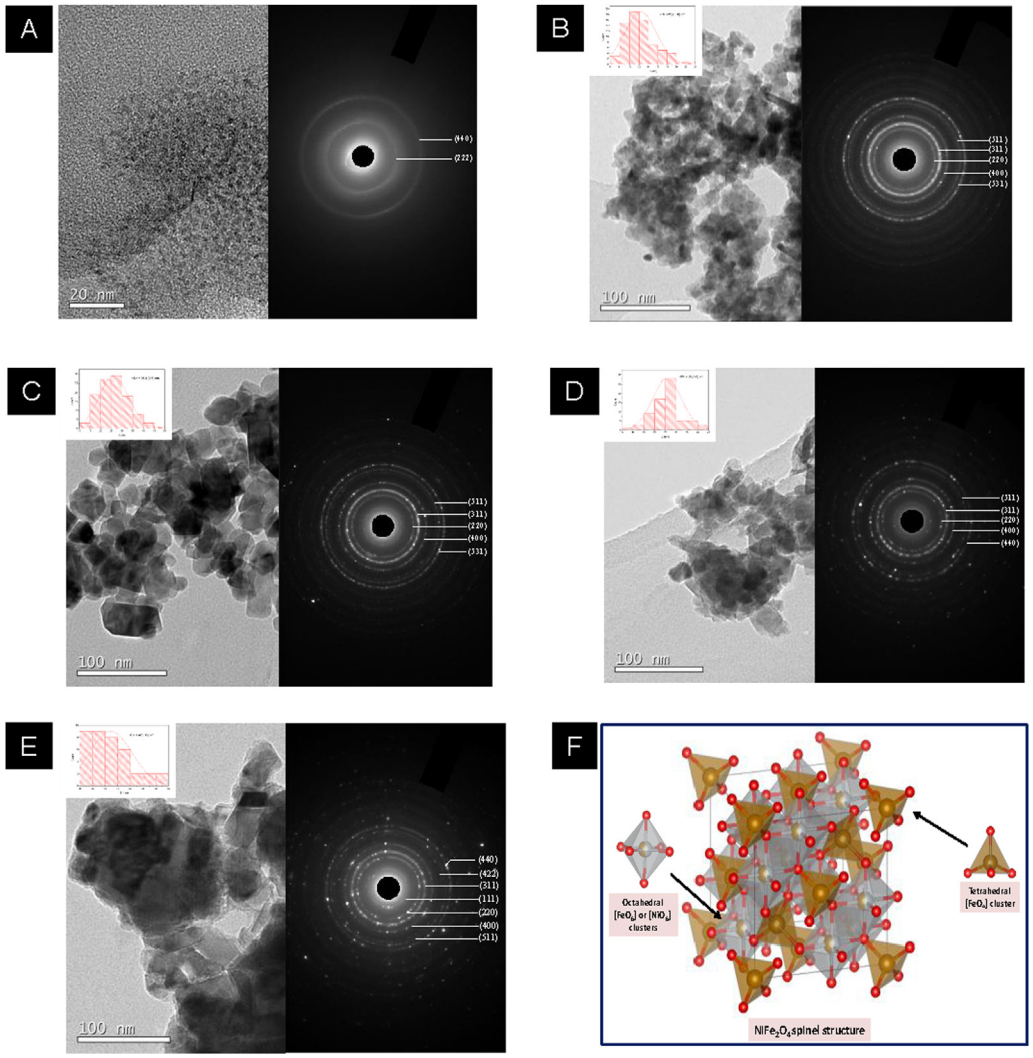

Fig. 2. TEM and SAED patterns of the as-prepared powders (a) and the powders heated at different temperatures: (b) NC700, (c) NC800, (d) NC900, and (e) NC1000 samples. (b-e) Inset showing the particle size distribution for samples heated at different temperatures. (f) Schematic representation of $NiFe_2O_4$ spinel structure.

Table 2
The weight and atomic observed by the EDS pattern analysis for these $NiFe_2O_4$ samples produced at various temperatures.

Samples	Element	Weight (%)	Atomic (%)	Fe/Ni
NC700	Fe K	42.24	24.49	1.58
	Ni K	28.11	15.51	
	O	29.64	60.00	
NC800	Fe K	48.44	28.00	2.33
	Ni K	21.82	12.00	
	O	29.74	60.00	
NC900	Fe K	44.08	25.53	1.76
	Ni K	26.25	14.47	
	O	29.67	60.00	
NC1000	Fe K	45.27	26.20	1.90
	Ni K	25.05	13.80	
	O	29.68	60.00	

field from 9 kOe, as shown in Fig. 3. All samples exhibit a predominant ferrimagnetic behavior. While that the inset in Fig. 3 reveals the magnetic behavior at the low field in the hysteresis loops, which indicate a permanent magnetization behavior for these samples in the temperature range studied. From these results, the values estimated of magnetic saturation (M_s) were obtained using the magnetization values obtained for fields above 9 kOe, we plotted the M x $1/H^2$ curve, we obtained an estimate for the saturation magnetization of the samples, coercivity (H_c) obtained from hysteresis loop are summarized in Table 3. These our results are consistent with the literature [40,41]. In this case, it is well established that the presence of oxygen vacancies in the $NiFe_2O_4$ spinel structure, in turn, can lead to the formation of magnetic moments [42,43]. Therefore, the difference observed between magnetic moment of the $[FeO_6]$, $[FeO_4]$ and $[NiO_6]$ clusters in the disordered lattice of $NiFe_2O_4$ spinel structure, in turn, has major contributed on the exchange coupling and magnetic properties of the samples as-prepared.

On the basis of these results, the magnetic measurements reveal a variation in the M_s and H_c that can in principle be attributed to grain growth by thermal annealing. In addition, the values of M_s is low (8.2 – 13.2 emu/g) in comparison with the room temperature M_s to the bulk $NiFe_2O_4$ (55 emu/g), as well as, a low H_c (34.6 – 177.1 Oe) with increasing of thermal annealing. It is attributed to the incomplete crystallization of small crystallite size, which in turn leads to the structural disorder on the surface of these nanoparticles since the spin disorder is high when the surface-to-volume ratio is large [42–44]. This is because the surface can behave as an inactive layer consequently the magnetization in this layer is negligible. Different from the room temperature samples, the ones calcined in low temperature conditions had a slight increase in their intensity with the temperature increase from 18.1 to 19.8 emu/g. Although those samples present similar behavior on their coercivity until 900 °C from (119.8 – 641.4 Oe) and at the highest temperature (1000 °C) a considerable decrease in their H_c value from

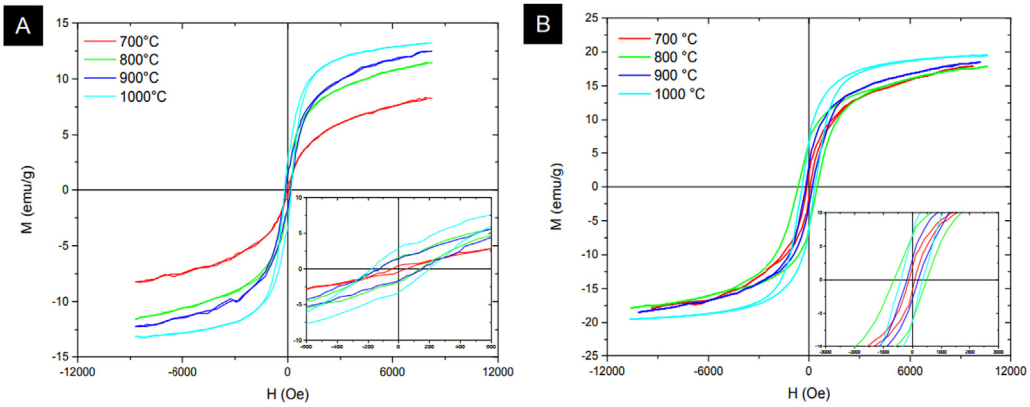

Fig. 3. Hysteresis loops (a) at room temperature and (b) at 7 K of $NiFe_2O_4$ nanoparticles.

Table 3
Coercive fields (H_C) and saturation magnetization (M_S) for as-prepared $NiFe_2O_4$ nanoparticles at room temperature and 7 K.

300 K			7 K	
Samples	**H_C (Oe)**	**M_S (emu/g)**	**H_C (Oe)**	**M_S (emu/g)**
NC700	34.6	8.7	119.8	18.1
NC800	118.4	12.1	186.2	18.2
NC900	118.4	12.9	641.4	18.7
NC1000	177.1	13.4	400.6	19.8

(641.4 – 400.6 Oe), in particular, these decrease is may be because of the formation of agglomerates that increase the average size of the particles, causing them to be larger than the critical single domain $NiFe_2O_4$ particles and they have a multidomain magnetic structure. Furthermore, with the grains growth the boundary volume decreases and the "pinning" effect of domain wall at the grain boundary is weakened with the annealing temperature [45,46]. These presented factors can result in the significant reduction of the H_c at higher temperatures.

3.3. Optical properties

UV–vis diffuse reflectance was used to determine the optical band gap for these samples by Tauc plots [47]. According to the literature [48], the $NiFe_2O_4$ materials have a direct optical band gap of about 2.7 eV. Fig. 4(a-d) shows the resulting spectra from the linear extrapolation of the $(F(R)h\nu)^{1/2}$ against photon energy ($h\nu$) of the Tauc plots. As results, the UV–vis measurements illustrate a variation in the optical band gap values from 1.35 eV to 1.43 eV for the $NiFe_2O_4$ powders heat-treated at different temperatures, in response to increasing the crystalline size (see Table 1) in good agreement with the literature [49–51]. In general, the optical band gap of a material is strong dependents of the degree of structural disorder in the lattice [52,53]. Finally, these results suggest the presence of new intermediate states in the interior of the band gap of the $NiFe_2O_4$ powders, in good agreement with our XRD results.

Fig. 5(a-e) illustrate the PL emission spectra at room temperature of $NiFe_2O_4$ powders obtained by co-precipitation method and heat-treated at different temperatures for 120 min, respectively. In particular, the PL spectra were deconvoluted in three components by using the Gaussian function, as shown in Fig. 5(b-e). Thus, considering that each component from the deconvoluted PL spectral a priori represents a different type of defect state in the forbidden gap that [53], in turn, are intimately related with the order-disorder effects on $NiFe_2O_4$ nanoparticles. Previous studies have showed that the PL emission band of Fe^{3+} is from the lowest excited $^4T_1(^4G)$ state onto the ground $^6A_1(^6S)$ state and the energy position of this PL emission band depends on the coordination of Fe^{3+} ions: in the case of tetrahedral coordination, the band maximum is observed in the red spectral region at 626–751 nm, and in the case of octahedral coordination, the band maximum is located in the near-infrared spectral region at 837–912 nm [54,55]. We consider that 690 and 820 nm emission peaks are due to is from the lowest excited $^4T_1(^4G) \rightarrow {}^6A_1(^6S)$ electronic transition of Fe^{3+} ion. In particular, the Fe^{3+} (d5) ions in both $[FeO_4]$, and $[FeO_6]$ clusters are in high-spin states [56]. While the bands around 439 nm and 483 nm are assigned to $^3T_1(^3P) \rightarrow {}^3A_2(^3F)$ and $^1T_2(^1D) \rightarrow {}^3A_2(^3F)$ transitions of Ni^{2+} in the octahedral sites [57–60]. Here, ones can observe that the peaks at 690 and 820 nm, associated with Fe^{3+} in tetrahedral site, disappear for higher calcination temperature. On the basis of these results, the it is well established that the broad emission centered in the green region of PL spectral, as shown in Fig. 5, is typical of a multiphonon process: that is, a system where relaxation occurs by several paths involving the participation of numerous states within the band gap of the material [61,62].

These states are related to the numerous kinds of defects directly associated with the degree of structural order-disorder. Hence, the changes observed in PL emission spectra of the $NiFe_2O_4$ powders, in principle, can reveal useful information regarding the different structural distortions that occurs on [O-Ni-O] and [O-Fe-O] bonds, and consequently promotes different levels of distortions on the $[NiO_6]$, $[FeO_4]$, and $[FeO_6]$ clusters. In order to quantification the effect of structural changes on the $NiFe_2O_4$ properties, as well as, reveal the underlying physical mechanism, particularly we used the Kröger–Vink notation to explain and represent the formation of defects inside the band gap as, for example, the presence of the oxygen vacancy (i.e., Vo^x, $Vo^{\bullet}$, and $Vo^{\bullet\bullet}$) in the $NiFe_2O_4$ systems, which are described in the following equations:

$$[NiO_6]^x + [NiO_5Vo^x] \rightarrow [NiO_6]' + [NiO_5Vo^{\bullet}] \quad (6)$$

$$[NiO_6]^x + [NiO_5Vo^{\bullet}] \rightarrow [NiO_6]' + [NiO_5Vo^{\bullet\bullet}] \quad (7)$$

$$[FeO_6]^x + [FeO_5Vo^x] \rightarrow [FeO_6]' + [FeO_5Vo^{\bullet}] \quad (8)$$

$$[FeO_6]^x + [FeO_5Vo^{\bullet}] \rightarrow [FeO_6]' + [FeO_5Vo^{\bullet\bullet}] \quad (9)$$

$$[FeO_4]^x + [FeO_3Vo^x] \rightarrow [FeO_4]' + [FeO_3Vo^{\bullet}] \quad (10)$$

$$[FeO_4]^x + [FeO_3Vo^{\bullet}] \rightarrow [FeO_4]' + [FeO_3Vo^{\bullet\bullet}] \quad (11)$$

Following the above logic, assuming that the $[NiO_6]$, $[FeO_6]$ and $[FeO_4]$ clusters are donors, while that the $[NiO_5Vo^{\bullet}]$, $[FeO_5Vo^{\bullet}]$ and $[FeO_4Vo^{\bullet}]$ clusters are donors/acceptors, and hence the $[NiO_5Vo^{\bullet\bullet}]$, $[NiO_5Vo^{\bullet\bullet}]$ and $[NiO_5Vo^{\bullet\bullet}]$ clusters are acceptors. We have also assumed that the charge redistribution may in principle lead to electron–hole recombination of localized excitons [61,62]. These results summarize the crucial role of structural disorder on the control of their physical and chemical behavior at the nanoscale, and hence creating exciting opportunities for the development of technological applications in the

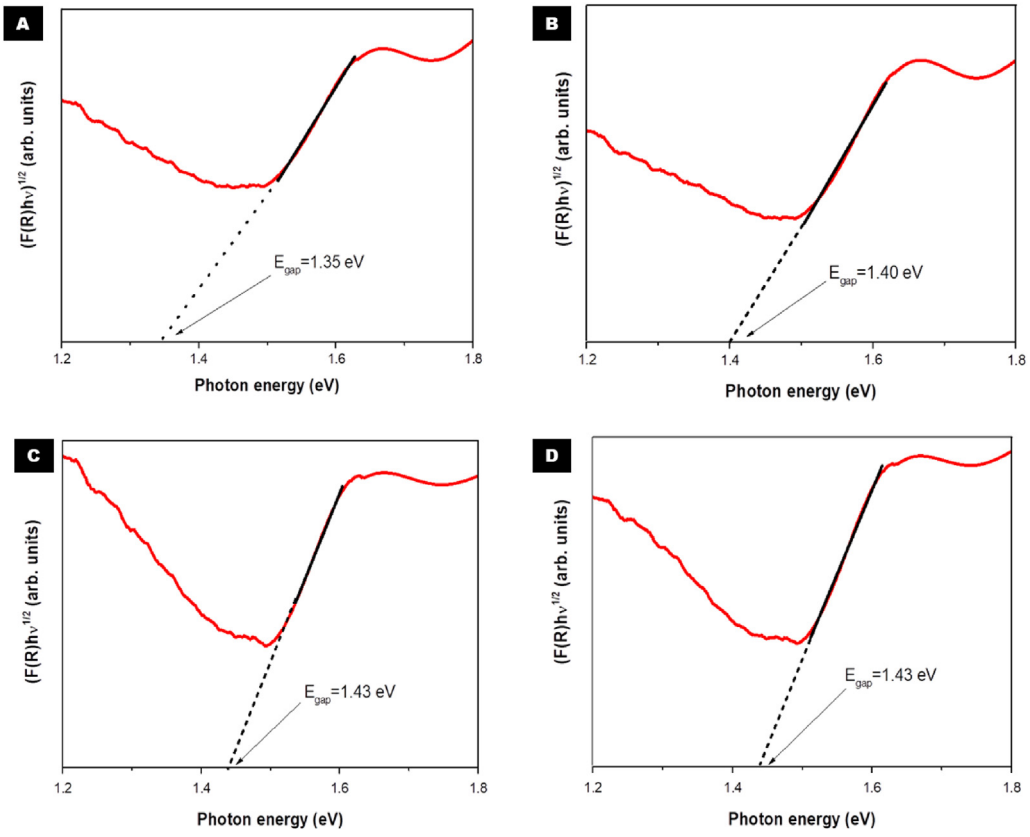

Fig. 4. UV–vis spectra for the $NiFe_2O_4$ powders heat-treated at: (a) 700 °C, (b) 800 °C, (c) 900 °C and (d) 1000 °C for 120 min, respectively.

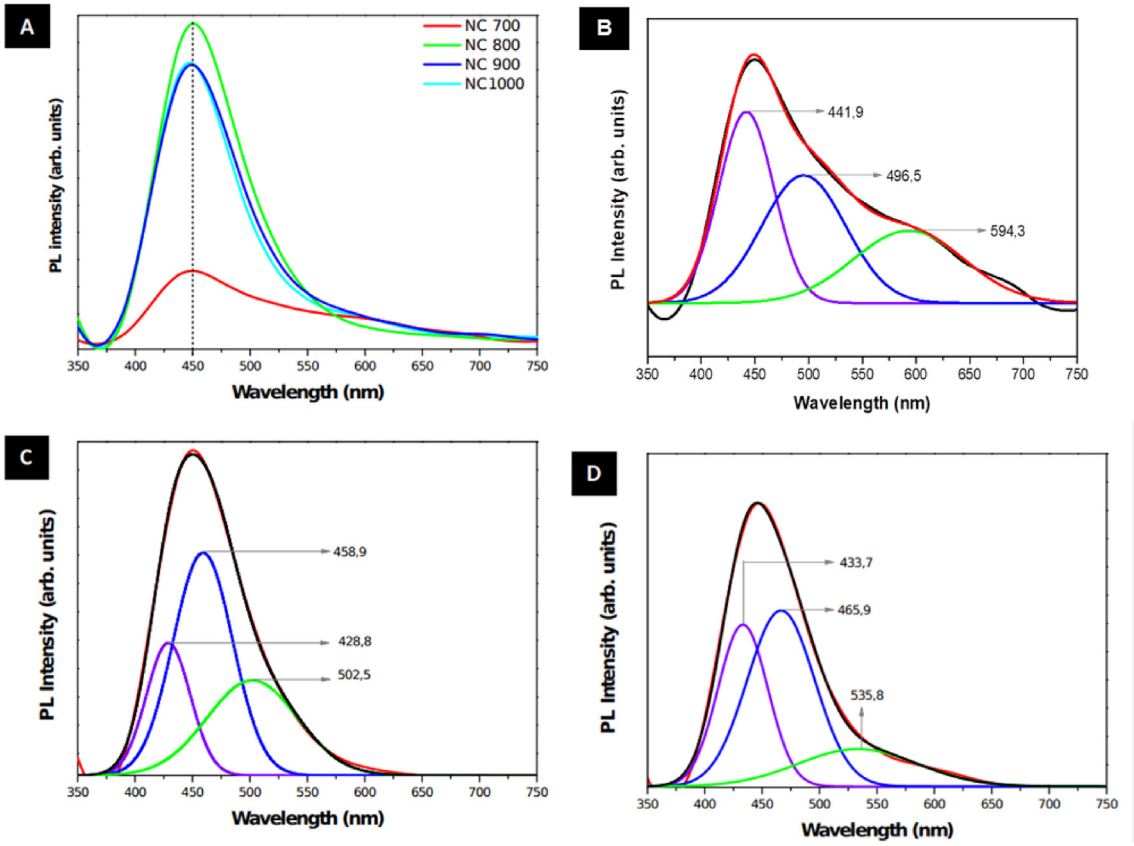

Fig. 5. (a) PL emission spectra for the NiFe2O4 powders heat-treated at different temperatures. Deconvoluted PL spectra for (b) NC700, (c) NC800, (d) NC900 and (e) NC1000 samples, respectively.

future based on these systems.

4. Conclusions

In conclusion, $NiFe_2O_4$ nanocrystals with tunable band gaps were prepared by the co-precipitation method and heat-treated at different temperatures. The study showed that all samples have an inverse spinel structure with high purity and crystallinity. For these samples, we also observed a predominant ferromagnetic behavior, as well as, a broad PL emission centered in the green region. A detailed analysis of these $NiFe_2O_4$ nanoparticles, in particular, reveals that these $[NiO_6]$, $[FeO_6]$ and $[FeO_4]$ clusters are highly disordered in the $NiFe_2O_4$ lattice, and hence clearly suggest that the magnetic and optical properties of the $NiFe_2O_4$ nanoparticles as-prepared are directly associated with localized states in the band gap. Additionally, the comprehension the structural changes and their effects on the properties of these nanocrystals, in turn, provides a set of design rules able to controlling properties of diverse materials at the nanoscale and hence have an enormous impact on the development of new technologies.

Acknowledgments

The authors are grateful to financial support of the Ministerio Español de Economia y Competitividad (MINECO) projects MAT2012–37109-C02-01 and MAT2013–48009-C4-1, Fundación Mutua Madrilena (FMM 2010), CNPQ (206.231/2014-8) and FAPESP (2013/07296-2).

References

[1] Q. Chen, P. Du, W. Huang, L. Jin, W. Weng, G. Han, Ferrite with extraordinary eletric and dieletric properties prepared from self - combustion technique, Appl. Phys. Lett. 90 (2007) 132907–132910.
[2] J. Hu, L.-s.Li, W. Yang, L. Manna, L.-w. Wang, A.P. Alivisatos, Linearly Polarized Emission from Colloidal Semiconductor Quantum Rods, Science 292 (2001) 2060–2063.
[3] M.A. Pena, J.L.G. Fierro, Chemical Structures and Performance of Perovskite Oxides, Chem. Rev. 101 (2001) 1981–2017.
[4] X. Wang, G. Yang, Z. Zhang, L. Yan, Synthesis of strong-magnetic nanosized black pigment $ZnxFe_{(3-x)}O_4$, J. Meng. Pigm. 74 (2007) 269–272.
[5] A.G. Abraham, et al., Enhanced magneto-optical and photo-catalytic properties of transition metal cobalt (Co^{2+} ions) doped spinel $MgFe_2O_4$ ferrite nanocomposites, J. Magn. Magn. Mater. 452 (2018) 380–388.
[6] A.G. Abraham, et al., Enhanced opto-magneto properties of $Ni_xMg_{1-x}Fe_2O_4$ ($0.0 \leq x \leq 1.0$) ferrites nano-catalysts, J. Nanoelectron. Optoe. 12 (2017) 1326–1333.
[7] I.J.C. Lynda, et al., Enhanced magneto-optical and photocatalytic properties of ferromagnetic $Mg_{1-y}Ni_yFe_2O_4$ ($0.0 \leq y \leq 1.0$) Spinel Nano-ferrites, J. Supercond. Nov. Magn. (2018) 1–11.
[8] V.M. Teresita, A. Manikandan, B. Avila Josephine, Electromagnetic properties and humidity-sensing studies of magnetically recoverable $LaMg_xFe_{1-x}O_{3-\delta}$ Perovskites nano-photocatalysts by sol-gel route, J. Supercond. Nov. Magn. 29 (2016) 1691–1701.
[9] A. Manikandan, J. Judith Vijaya, L. Joh Kennedy, Structural, optical and magnetic properties of porous α-Fe_2O_3 nanostructures prepared by rapid combustion method, J. Nanosci. Nanotech. 13 (2013) 2986–2992.
[10] M.F. Valan, A. Manikandan, S. Arul Antony, A novel synthesis and characterization studies of magnetic Co_3O_4 nanoparticles, J. Nanosci. Nanotech. 15 (2015) 4580–4586.
[11] J.A. Mary, et al., Structure and magnetic properties of Cu-Ni alloy nanoparticles prepared by rapid microwave combustion method, Trans. Nonferrous Met. Soc. China 24 (2014) 1467–1473.
[12] S. Jayasree, A. Manikandan, A.M. Mohideen, C. Barathiraja, S.A. Antony, Comparative study of combustion methods, opto-magnetic and catalytic properties of spinel $CoAl_2O_4$ nano- and microstructures, Adv. Sci. Eng. Med. 7 (2015) 672–682.
[13] J. Jacob, M. Abdul Khadar, VSM and Mössbauer sutudy of nano structured hematite, J. Magn. Magn. Mater. 322 (2010) 614–621.
[14] E. Roduner, Size matters: why nanomaterials are different, Chem. Soc. Rev. 35 (2006) 583–592.
[15] S. Josh, M. Kumar, S. Chhoker, G. Srivastava, M. Jewariya, V.N. Singh, Structural, magnetic, dieletric and optical properties of nickel ferrite nanoparticles sythesized by co-precipitation method, J. Mol. Struct. 1076 (2014) 55–62.
[16] A. Alarifi, N.M. Deraz, S. Shaban, Structural, morphological and magnetic properties of $NiFe_2O_4$ nano-particles, Compd 486 (2009) 501–506.
[17] J.L. Gunjakar, A.M. More, K.V. Gurav, C.D. Lokhande, Chemical synthesis of spinel nickel ferrite ($NiFe_2O_4$) nano-sheets, Appl. Surf. Sci. 254 (2008) 5844–5848.
[18] L. Chauhan, A.K. Shukla, K. Sreenivas, Dieletric and magnetic properties of Nickel ferrite ceramics using crystallyne powders derived from DL alanine fuel in sol-gel auto-combustion, Ceram. Int. 41 (2015) 8341–8351.
[19] C. Kim, Growth of ultrafine Co-Mn ferrite and magnetic properties by a sol-gel method, J. Appl. Phys. 85 (1999) 5223–5225.
[20] Y.I. Kim, D. Kim, C.S. Lee, Synthesis and characterization of $CoFe_2O_4$ magnetic nanoparticles prepared by temperature-controlled coprecipitation method, Phys. B 337 (2003) 42–51.
[21] J.F. Hochepied, P. Bonville, M.P. Pileni, Nonstoichiometric zinc ferrite nanocrystals: syntheses and Unusual Magnetic Properties, J. Phys. Chem. B. 104 (2000) 905–912.
[22] N. Feltin, M.P. Pileni, New technique for synthesizing iron ferrite magnetic nanosized particles, Langmuir 13 (1997) 3927–-3933.
[23] Y. Shi, J. Ding, X. Liu, J. Wang, $NiFe_2O_4$ ultrafine particles prepared by co-precipitation/mechanical alloying, J. Magn. Magn. Mater. 205 (1999) 249–254.
[24] R.S. Yadav, J.H.J. Masilko, L. Kalina, J. Wasserbauer, M. Hajdúchová, V. Enev, I. Kuřitka, Z. Kozakova, Effects of annealing temperature variation on the evolution of structural and magnetic properties of $NiFe_2O_4$ Nanoparticles synthesized by starch assisted sol-gel auto-combustion method, J. Magn. Magn. Mater. 394 (2015) 439–447.
[25] H. Li, H.-z. Wu, G.-x. Xiao, Effects of synthetic conditions on particle size and magnetic properties of $NiFe_2O_4$, Powder Technol. 198 (2010) 157–166.
[26] E. Longo, F. La Porta, Recent Advances in Complex Functional Materials: From Design to Application, Springer, Gewerbestrasse, CHE, 2017.
[27] R. Massart, Preparation of aqueous magnetic liquids in alkaline and acidic media, IEEE Trans. Magn. 17 (1981) 1247–1248.
[28] R. Raeisi Shahraki, M. Ebrahimi, S.A. Seyyed Ebrahimi, S.M. Masoudpanah, Structural characterization and magnetic properties of superparamagnetic zinc ferrite nanoparticles synthesized by the coprecipitation method, J. Magn. Magn. Mater. 324 (2012) 3762–3765.
[29] H. Rietveld, Aprofile refinement method for nuclear and magnetic structures, J. Appl. Crystallogr. 2 (1969) 65–71.
[30] J. Rodriguez-Carvajal, Recent advances in magnetic structure determination by neutron powder diffraction, Phys. B 192 (1993) 55–69.
[31] J.F.D.F. Araujo, M.C. Costa, S.R.W. Louro, A.C. Bruno, A portable Hall magnetometer probe for characterization of magnetic iron oxide nanoparticles, J. Magn. Magn. Mater. 426 (2017) 159–162.
[32] M. Amir, H. Gungunes, A. Baykal, et al., Effect of annealing temperature on magnetic and mossbauer properties of $ZnFe_2O_4$ nanoparticles by sol-gel approach, J. Supercond. Nov. Magn. (2018) 1–10.
[33] S. Asiri, M. Sertkol, H. Güngüneş Md. Amir, A. Manikandan, İ. Ercan, A. Baykal, The temperature effect on magnetic properties of NiFe2O4 nanoparticles, J. Inorg. Organomet. Polym. (2018) 1–11.
[34] A. Silambarasu, A. Manikandan, K. Balakrishnan, Room-temperature superparamagnetism and enhanced photocatalytic activity of magnetically reusable spinel $ZnFe_2O_4$ nanocatalysts, J. Supercond. Nov. Magn. 30. 9 (2017) 2631–2640.
[35] M.H. Habibi, F. Fakhri, Hydrothermal synthesis of nickel iron oxide nano-composite and application as magnetically separable photocatalyst for degradation of Solar Blue G dye, J. Mater. Sci. – Mater. El. 28 (2017) 14091–14096.
[36] Z.K. Karakaş, R. Boncukcuoğ- lu, I.H. Karakaş, M. Ertuğrul, The effects of heat treatment on the synthesis of nickel ferrite ($NiFe_2O_4$) nanoparticles using the microwave assisted combustion method, J. Magn. Magn. Mate. R. 374 (2017) 298–306.
[37] JCPDS-International Centre for Diffraction Data, 2015.
[38] T. Prabhakaran, J. Hemalatha, Chemical control on the size and properties of nano $NiFe_2O_4$ synthesized by sol–gel autocombustion method, Ceram. Int. 40 (2014) 3315–3324.
[39] H. Li, H.-z. Wu, G-x Xiao, Effects of synthetic conditions on particle size and magnetic properties of $NiFe_2O_4$, Powder Technol. 198 (2010) 157–166.
[40] L. Wang, H. Dong, J. Li, J. Hua, S. Xu, M. Feng, H. Li, Effects of annealing temperature on structural and magnetic properties of $Ni_{0.8}Zn_{0.2}Fe_2O_4$ thin films, Ceram. Int. 40 (2014) 10323–10327.
[41] P. Laokul, V. Amornkitbamrung, S. Seraphin, S. Maensiri, Characterization and magnetic properties of nanocrystalline $CuFe_2O_4$, $NiFe_2O_4$, $ZnFe_2O_4$ powders prepared by the Aloe vera extract solution, Curr. Appl. Phys. 11 (2011) 101–108.
[42] V. Fernandes, R.J.O. Mossanek, P. Schio, J.J. Klein, A.J.A. de Oliveira, W.A. Ortiz, N. Mattoso, J. Varalda, W.H. Schreiner, M. Abbate, D.H. Mosca, Dilute-defect magnetism: origin of magnetism in nanocrystalline CeO_2, Phys. Rev. B 80 (2009) 035202.
[43] L.K.S. Herval, D. von Dreifus, A.C. Rabelo, A.D. Rodrigues, E.C. Pereira, Y.G. Gobato, A.J.A. de Oliveira, M.P.F. de Godoy, The role of defects on the structural and magnetic properties of Nb_2O_5, J. Alloy. Compd. 653 (2015) 358–362.
[44] Y.-W. Jun, J.-W. Seo, Nanoscaling laws of magnetic nanoparticles and their applicabilities in biomedical sciences J. Cheon, J. Acc. Chem. Res. 41 (2008) 179–189.
[45] S. Song, Q. Song, J. Li, M.V. Ramana, Z. Zhang, Characterization of submicrometer-sized NiZn ferrite prepared by spark plasma sintering, Hydrothermal synthesis of $NiFe_2O_4$ nano-particles: structural, morphological, optical, electrical and magnetic properties, Ceram. Int. 40 (2014) (2014) 6473–6479.
[46] K.C.B. Naidu, W. Madhuri, Hydrothermal synthesis of $NiFe_2O_4$ nano-particles: structural, morphological, optical, electrical and magnetic properties, Bull. Mater. Sci. 40 (2017) 417–425.
[47] J. Tauc, Optical properties and eletronic structure of amorphous Ge and Si, Mater. Res. Bull. 3 (1968) 37–46.
[48] H. Perron, T. Mellier, C. Domain, J. Roques, E. Simoni, R. Drot, H. Catalette, Structural investigation and electronic properties of the nickel ferrite $NiFe_2O_4$: a periodic density functional theory approach, J. Phys.: Condens. Matter 19 (2007) 346219–346229.

[49] S. Asiri, M. Sertkol, S. Guner, H. Gungunes, K.M. Batoo, T.A. Saleh, A. Baykal, Hydrothermal synthesis of $Co_yZn_yMn_{1-2y}Fe_2O_4$ nanoferrites: magneto-optical investigation, Ceram. Int. 44 (2018) 5751–5759.
[50] A. Manikandan, E. Manikandan, B. Meenatchi, J. S, et al., Rare earth element (REE) lanthanum doped zinc oxide (La: zno) nanomaterials: synthesis structural optical and antibacterial studies, J. Alloy. Compd. 723 (2017) 1155–1161.
[51] S. Suguna, S. Shankar, S.K. Jaganathan, et al., Novel synthesis of spinel Mn x Co1 − x Al2 *O* 4 (x = 0.0 to 1.0) nanocatalysts: effect of Mn2+ doping on structural, morphological, and opto-magnetic properties, J. Supercond. Nov. Magn. 30 (2017) 691–699.
[52] F.M.C. Batista, F.A. La Porta, L. Gracia, E. Cerdeiras, L. Mestres, M. Siu, Li, N.C. Batista, J. Andrés, E. Longo, L.S. Cavalcante, A joint experimental and theoretical study on the electronic structure and photoluminescence properties of $Al_2(WO_4)_3$ powders, J. Mol. Struct. 1081 (2015) 381–388.
[53] F.A. La Porta, J. Andres, M.V.G. Vismara, C.F.O. Graeff, J.R. Sambrano, M.S. Li, J.A. Varela, E. Longo, Correlation between structural and electronic order–disorder effects and optical properties in ZnO nanocrystals, J. Mater. Chem. C. 2 (2014) 10164–10174.
[54] D. Berger, A.P. de Moura, L.H. Oliveira, W.B. Bastos, F.A. La Porta, I.L.V. Rosa, M.S. Li, S.M. Tebcherani, E. Longo, J.A. Varela, Improved photoluminescence emission and gas sensor properties of ZnO thin films, Ceram. Int. 42 (2016) 13555–13561.
[55] I.N. Ogorodnikov, V.A. Pustovarov, S.A. Yakovlev, L.I. Isaenko, Spectroscopic study of red-light-emitting centers in $K_2Al_2B_2O_7$: Fe single crystals, Opt. Mater. 35 (2013) 1173–1178.
[56] L. Alyabyeva, V. Burkov, B. Mill, Optical spectroscopy of $La_3Ga_5SiO_{14}$ disordered crystals doped with Fe^{3+} ions, Opt. Mat. 43 (2015) 55–58.
[57] R.C. Rai, S. Wilser, M. Guminiak, B. Cai, M.L. Nakarmi, Optical and electronic properties of $NiFe_2O_4$ and $CoFe_2O_4$ thin films, Appl. Phys. A 106 (2012) 207–211.
[58] E.P. Dubrovina, V.A. Sandulenko, M.I. Demchuk, N.V. Kuleshov, V.P. Mikhailov, The optical spectroscopy of Ni-doped garnets, Chem. Phys. Lett. 170 (1990) 473–477.
[59] E. Zannoni, E. Cavalli, A. Toncelli, M. Tonelli, M. Bettinelli, Optical spectroscopy of $Ca_3Sc_2Ge_3O_{12}$: Ni_{21}, J. Phys. Chem. Solids 60 (1999) 449–455.
[60] S. Joshi, M. Kumar, S. Chhoker, G. Srivastava, M. Jewariya, V.N. Singh, Structural, magnetic, dielectric and optical properties of nickel ferrite nanoparticles synthesized by co-precipitation method, J. Mol. Struct. 1076 (2014) 55–62.
[61] A.P. de Moura, L.H. de Oliveira, I.L.V. Rosa, C.S. Xavier, P.N. Lisboa-Filho, M.S. Li, F.A. La Porta, E. Longo, J.A. Varela, Structural, optical, and magnetic properties of $NiMoO_4$ nanorods prepared by microwave sintering, Sci. World J. 2015 (2015) 8.
[62] L.H. Oliveira, A.P. de Moura, F.A. LA Porta, I.C. Nogueira, E.C. Aguiar, T. Sequinel, I.L.V. Rosa, E. Longo, J.A. Varela, Influence of Cu-doping on the structural and optical properties of $CaTiO_3$ powders, Mater. Res. Bull. 81 (2016) 1–9.